Large sliding contact along branched discontinuities with X-FEM

Maximilien Siavelis, Martin Guiton, Patrick Massin, Nicolas Moës

Large sliding contact along branched discontinuities with X-FEM

Maximilien Siavelis · Martin L. E. Guiton · Patrick Massin · Nicolas Moës

Abstract The extended finite element method (X-FEM) has been developed to minimize requirements on the mesh in a problem with a displacement discontinuity. We present the development carried out to take advantage of the X-FEM approach in simplifying the meshing of complex 3D networks of discontinuities with junctions. Contact with large sliding along the branched discontinuities is discussed. Solu-tions are proposed and discussed to solve some matrix condi-tioning issues. Several examples are presented in this paper in order to prove the efficiency of the proposed approach.

Keywords X-FEM · Contact · Large sliding · Junction

M. Siavelis (✉) · M. L. E. Guiton
IFPEN, 1 à 4 Avenue de Bois-Préau, 92852 Rueil-Malmaison Cedex, France
e-mail: maximilien.siavelis@centraliens-nantes.net

Present Address:
M. Siavelis
LaMSID, UMR EDF-CNRS-CEA 2832, 1 Avenue du Général de Gaulle, 92141 Clamart, France

Present Address:
M. L. E. Guiton
Applied Mechanics Division, IFPEN, Rond-point de l'échangeur de Solaize, BP 3, 69360 Solaize, France
e-mail: martin.guiton@ifpen.fr

P. Massin
LaMSID, UMR EDF-CNRS-CEA 2832, 1 Avenue du Général de Gaulle, 92141 Clamart, France
e-mail: patrick.massin@edf.fr

N. Moës
GeM, Ecole Centrale de Nantes, UMR CNRS 6183, 1 rue de la Noë, 44321 Nantes Cedex 3, France
e-mail: nicolas.moes@ec-nantes.fr

1 Introduction

Building 3D meshes for industrial structures is difficult, especially when the mesh has to conform to complex geometries with discontinuous surfaces. In this work we are interested in the extended finite element method (X-FEM) which represents a discontinuity thanks to an enrichment of the nodal degrees of freedom (d.o.f.) and thus facilitates the model design [23]. We focus on the case of branched discontinuities. Two types of approaches have been proposed to take into account branched cracks with X-FEM. The first one, given by [8], proposes to add to the classical X-FEM enrichment a junction enrichment over the branched discontinuities. The advantage of this approach is to simplify the implementation if one wants to model crack fronts. The disadvantage is that the introduction of the discontinuities have to respect a certain hierarchy. The second one, given by [37], is more general and easier to implement. Based on GFEM, each discontinuity is independent from the others and no junction enrichment is needed. A sequential automated procedure is given to model closed discontinuities like grains in polycrystals. The principle is to loop on the discontinuities. A d.o.f. enrichment is added for each node intersected by the discontinuity. Then, to recover the partition of unity for each multi-enriched node, the last added d.o.f. is removed. Notice that the generalization to crack fronts is not as simple [11].

A few formulations are proposed to treat contact with X-FEM in a small sliding context, with penalty regularization [10,18,22] or with Lagrangian regularization [4,17,31]. With X-FEM, a naive linear $P1$–$P1$ interpolation choice for the displacement and contact spaces, respectively (i.e. with a contact d.o.f. located at a cut edge) is not stable and implies oscillations [16,25]. When modeling contact conditions with a mixed method involving Lagrange multipliers, particular attention should be paid to the choice of the discrete space

of dual unknowns with respect to the displacement space. The latter should typically not be less than the former, if one wants to satisfy the LBB condition [6] which ensures the existence and uniqueness of the solution [2]. A way to recover the satisfaction of this condition with X-FEM is to enrich the displacement, for example with bubble interpolation functions [26]. Another possibility is to reduce the dual space by an algorithm that selects a subset from the set of cut edges. Each selected edge is called a vital edge and only these hold a Lagrange multiplier [25]. To provide a better approximation of the pressure space, this algorithm was improved in [17], in which a numerical validation for the LBB condition as in [7] is given. The introduction of contact d.o.f. at cut edges complicates the numerical implementation by introducing additional pseudo-nodes located at the middle of the edges. In [17], for the elements either intersected by a discontinuity or with an edge along the discontinuity, the Lagrange interpolation is defined in between the intersection points or on the interface of the element edge, respectively. Hence, the Lagrange interpolation differs from the displacement interpolation which uses the element nodes. This difference makes it difficult to obtain an analytical proof of satisfaction of the LBB condition even if the numerical proof is held. For that reason the vital edge based formulation of [4], which gives an analytical proof of the LBB condition satisfaction for 2D triangular meshes, proposes to interpolate the contact pressure using element nodes, as for the displacements.

The extension to large sliding was developed in [29], by considering that each integration of a contact contribution is associated to a special contact element based on a master–slave approach as in [5]. The difference with FEM contact elements is that slave and master elements are no more constituted by elements discretizing the interface but are built with enriched bulk elements. It is then possible to update the master–slave association with the sliding, within a fixed point algorithm. To treat contact over a junction, [33] propose an approach that uses the GFEM enrichment of [37] with the contact formulation of [26] to model complicated geometries with triple interface junctions.

In the present paper, we follow the approach of [8] to provide a new implementation of X-FEM which aims at describing large sliding contact along discontinuities which can branch sequentially. The paper is organized as follows. In Sect. 2, we recall the contact formulation of [5], based on an augmented Lagrangian solved with a Generalized Newton algorithm as in [1]. In Sect. 3, we describe a possible implementation of the approach of [8] that extends the formulation to a complex network of 3D discontinuities. In Sect. 4, we present the extension of the junction approach to contact, based on the vital edge selection approach of [17]. As in [4], the contact unknowns are interpolated with respect to nodal values. For the extension to large sliding, the approach of [29] extended to 3D problems in [35] is used to perform a master–slave pairing. In Sect. 5, solutions to solve matrix conditioning issues are discussed. A stiffness conditioning criterion and the orthogonalization of [3] are tested. Finally in Sect. 6, several applications are presented to illustrate the potential of the method.

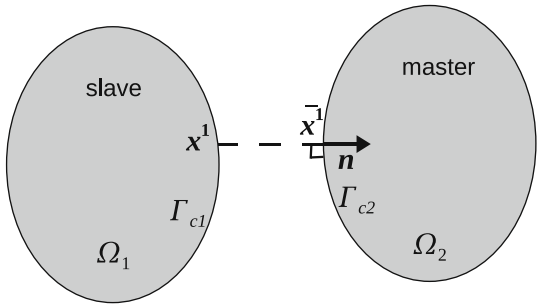

Fig. 1 $\mathbf{x}^1$ belongs to the slave surface Γ_{c1}, $\bar{\mathbf{x}}^1$ is the projection of $\mathbf{x}^1$ on the master surface Γ_{c2}

2 Mixed continuous formulation of contact

2.1 Variational forms

The displacement can be large, especially along the discontinuity interface, but small strains are assumed as well as an elastic constitutive law. The generalization to finite rotations with small strain kinematics used in some examples of Sect. 6 does not present any difficulty.

Let us denote by Ω the domain of interest whose boundaries are composed of a part Γ_u, Γ_t and Γ_c where conditions are imposed on the displacement $\mathbf{u}$, on the pressure distribution and to satisfy contact, respectively. In this paper, we assume Γ_c to represent a discontinuity with interfacial boundaries Γ_{c1} and Γ_{c2} (see Fig. 1). Considering the inward normal $\mathbf{n}$ to Γ_{c2}, we can write the frictionless contact force per unit surface $\mathbf{r}$ that Ω_2 applies to Ω_1 where λ is negative and represents the contact reaction pressure:

$$\mathbf{r} = \lambda \mathbf{n}. \tag{1}$$

Following the usual convention (see for instance [40]), contact is generally imposed on a slave surface, here denoted Γ_{c1}, with respect to a master surface Γ_{c2}, by introducing the normal distance between a slave point $\mathbf{x}^1$ and its projection $\bar{\mathbf{x}}^1$ on Γ_{c2}:

$$d_n = (\mathbf{x}^1 - \bar{\mathbf{x}}^1) \cdot \mathbf{n}. \tag{2}$$

When considering the spatial discretization of two surfaces which could come into contact during the deformation, the choice of which surface should be the slave may respect several conditions to guarantee the validity of the numerical solution [40]). In particular, the master surface should be

supported by the less deformable body or should be the one with the coarsest mesh to avoid part of the master surface with free conditions. Such guidelines are not useful for the X-FEM approach presented in this paper, since the two bodies may be deformable and the meshes of the contacting surface are initially coincident. The choice of the slave surface will then be arbitrary.

The Signorini contact conditions read:

$$\lambda \leq 0, \quad d_n \leq 0, \quad \lambda d_n = 0. \tag{3}$$

Following [5], an augmented Lagrangian regularization is used with the augmented multiplier:

$$g_n = \lambda - \rho_n d_n, \tag{4}$$

where ρ_n is a positive scalar with dimensions of a pressure over a displacement. We also introduce χ, the $\mathbb{R}^-$ indicator function, in order to rewrite the system of equations and inequalities (3) as:

$$\lambda - \chi\,(g_n)\, g_n = 0. \tag{5}$$

Taking into account the augmented Lagrangian, the contact reaction is then represented by $\chi(g_n)g_n$. The variational form of the equilibrium, for any variation of displacement $\mathbf{u}^*$ that belongs to the space of kinematically admissible fields reads:

$$\int_{\Omega} \sigma(\boldsymbol{\epsilon}(\mathbf{u})) : \boldsymbol{\epsilon}(\mathbf{u}^*) d\Omega - \int_{\Gamma_c} \chi(g_n) g_n \mathbf{n} \cdot [\![\mathbf{u}^*]\!] d\Gamma = L_{meca}(\mathbf{u}^*), \tag{6}$$

where $[\![\mathbf{u}]\!] = \mathbf{u}(x^1) - u(\bar{\mathbf{x}}^1)$. The first term is the contribution from the virtual internal work, denoted as the double product between the Cauchy stress tensor $\boldsymbol{\sigma}$ and the virtual strain ϵ and the second term is related to the work of contact forces. The right hand side term L_{meca} of Eq. (6) represents the possible contribution from the body force and applied pressure on Γ_t which are not of interest in this paper. Finally, the formulation of [5] is mixed in terms of pressure and displacements and the variational form of the contact conditions given by Eq. (5) for all variations of λ^* reads:

$$\int_{\Gamma_c} -\frac{1}{\rho_n} \left(\lambda - \chi(g_n) g_n\right) \lambda^* d\Gamma = 0. \tag{7}$$

2.2 Iterative algorithm for non linearities

Algorithm 1 shows the strategy to take into account non linearities. The external loop concerns the geometry change. For each geometric configuration, a fixed point on the change of slave–master contact association during large sliding is performed. Note that the unit normal vector $\mathbf{n}$ which carries the normal contact reaction is fixed during an iteration of this loop. The second inner loop is a fixed point on the contact status, i.e. $\chi(g_n)$, as in [13]. Finally, the Newton–Raphson loop is achieved thanks to a tangent operator obtained after linearization of Eqs. (5) and (6). See [5] for the detailed expressions.

Algorithm 1 Iterative algorithm on each geometric configuration.

- Fixed point on slave–master association and contact basis
  - Fixed point on contact status
    - Loop on Newton–Raphson iterations (geometric non linearities)

3 Multiple branched discontinuities with the X-FEM

The main idea of the X-FEM, detailed in [23], is to avoid remeshing by proposing instead the construction of an enriched approximation of the kinematic fields resulting from the intersection between the geometry of the discontinuities and the mesh. A standard finite element approximation is enriched in the neighborhood of the discontinuity by local functions related to additional d.o.f. We consider the normal level set ψ_n as the signed distance of the projection on the discontinuity surface or its tangential extension and the tangential level set ψ_τ as the distance of this projection to the crack front. The discontinuity surface is then represented by the iso-zero of ψ_n and the crack front by the intersection of the iso-zero of the two level sets ψ_n and ψ_τ. The finite element approximation can be written:

$$\mathbf{u}(\mathbf{X}) = \sum_{i \in N_{\mathbf{X}}} \mathbf{a}_i \phi_i(\mathbf{X}) + \sum_{j \in J} \mathbf{b}_j \phi_j(\mathbf{X}) H(\psi_n(\mathbf{X})) + \sum_{k \in K} \sum_{\alpha=1}^{4} \mathbf{c}_{\alpha,k} \phi_k(\mathbf{X}) F_\alpha(\psi_n(\mathbf{X}), \psi_\tau(\mathbf{X})) \tag{8}$$

where $N_{\mathbf{X}}$ is the set of nodes of the element containing point $\mathbf{X}$; $\mathbf{a}_i$ is the classical d.o.f. at node i; $\phi_i(\mathbf{X})$ is the shape function associated with node i; $J \subset N_{\mathbf{X}}$ is the subset of nodes enriched by the generalized Heaviside function H. A node j is enriched with $\mathbf{b}_j$ if the support of its associated shape function is totally cut by the discontinuity; $K \subset N_{\mathbf{X}}$ is the subset of nodes enriched by the asymptotic functions F_α. A node k is enriched with $\mathbf{c}_{\alpha,k}$ if the support of its associated shape function is partially cut by the discontinuity (i.e. it contains a crack front). The generalized Heaviside function H is a discontinuous function across the discontinuity with constant value $+1$ on one side and -1 in the other side. The asymptotic functions F_α are given by:

$$\mathbf{F} = \left\{ \sqrt{r} \sin\frac{\theta}{2}, \sqrt{r} \cos\frac{\theta}{2}, \sqrt{r} \sin\frac{\theta}{2} \sin\theta, \sqrt{r} \cos\frac{\theta}{2} \sin\theta \right\} \tag{9}$$

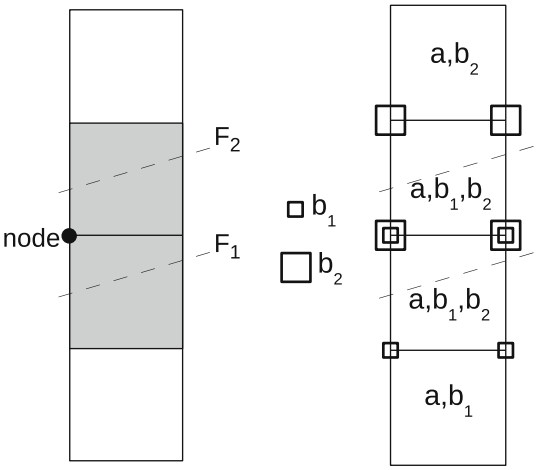

Fig. 2 Type of elements generated for a node support (*gray*) cut by two discontinuities (*left*) and nodal enrichment associated to both discontinuities (b_1 and b_2 d.o.f.) (*right*)

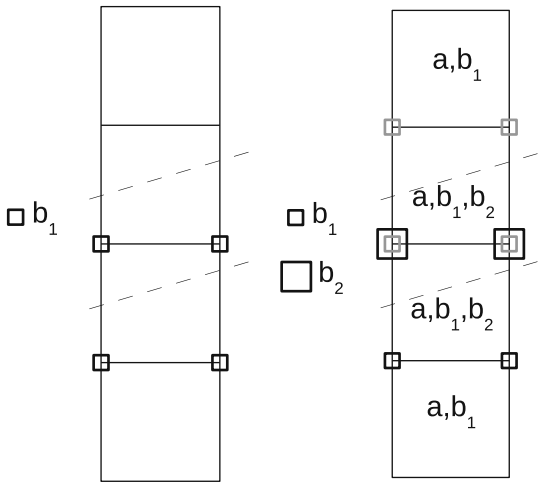

Fig. 3 Sequential enrichment. Introduction of the first (*left*) and second (*right*) discontinuities

where (r, θ) is the position of point $\mathbf{X}$ associated to the crack front polar basis, that can be easily expressed in terms of the local values of ψ_n and ψ_τ [24].

In this part we describe a possible implementation of the branched crack approach of [8] which extends the junction formulation to multiple branched discontinuities for a 3D complex network.

3.1 Multiple Heaviside enrichment

The first difficulty is to associate several enrichment d.o.f. for a node which has its support cut by several discontinuities. The first idea is to associate the name of the d.o.f. to the name of the discontinuity. For example in Fig. 2, the support of the represented node is cut by the discontinuities F_1 and F_2. We associate a b_1 d.o.f. for the Heaviside function of F_1 and a b_2 d.o.f. for the Heaviside function of F_2. The disadvantage of this approach is the loss of a generic d.o.f. name in generic elements to simplify the assembly of the linear associated system.

To generate a reduced number of d.o.f., the second idea is to dissociate the d.o.f. name from the discontinuity name. An automatic enrichment is performed by Algorithm 2. The principle is to introduce sequentially the discontinuities. If a node has to be enriched by a discontinuity, we increment the d.o.f. number for this node (see Fig. 3). The name corresponding to the d.o.f. does not correspond anymore to the name of the discontinuity, but we introduce a data structure that is able to link the d.o.f. name to the discontinuity name during the procedure. Then, the second term of the right member of Eq. (8) can be rewritten as:

$$\sum_{j \in J} \phi_j(\mathbf{X}) \sum_{i_H=1}^{n_H} \mathbf{b}_{i_H,j} H(\psi_{n_F}(\mathbf{X})), \tag{10}$$

where n_H is the total number of Heaviside d.o.f. at node j; F is the discontinuity name associated to the d.o.f. $\mathbf{b}_{i_H}$ at node j.

Algorithm 2 Sequential enrichment algorithm.

- the number of Heaviside enrichment is initialized to zero for all mesh nodes
- loop on the discontinuities
  - loop on the mesh nodes
    - if the node is enriched by the discontinuity:
      -we increment the number of Heaviside d.o.f.
      -the current d.o.f. number for the node is associated to the current discontinuity

3.2 Sequential cutting into sub-elements

The Gauss–Legendre integration requires continuous domains or specific integration manipulations as in [39]. If an element is cut by several discontinuities, we need to divide the element into sub-elements that conform to the different discontinuities. We adopt the sequential cutting algorithm of elements into sub-elements described in Algorithm 3. First, an element is subdivided into simple sub-elements. A quadrangle is for example subdivided into two triangles and an hexahedron into six tetrahedra. Then, if a sub-element is cut once, it is divided into sub-elements. If it is cut twice, a cut sub-element is subdivided a second time. Figure 4 illustrates the procedure for an element cut by two discontinuities.

The approach is not limited by the number of discontinuities that cross an element. Nevertheless, the number of generated sub-elements is not optimal and can imply an important number of associated integration points. For example in Fig. 5, if we group by area the sub-elements that have the same Heaviside functions, we need a number of

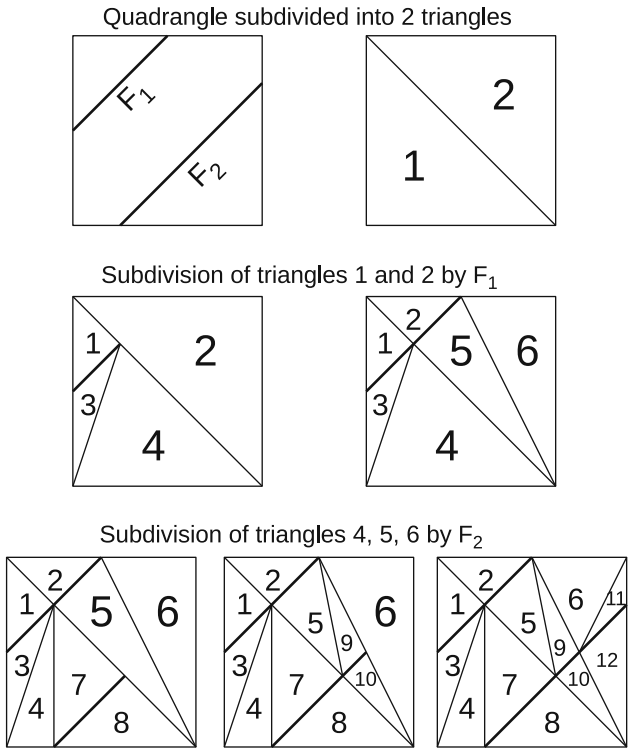

Fig. 4 Sub-elements generated in an element cut by two discontinuities

Algorithm 3 Sequential procedure for multi-cutting.

- considering an X-FEM element
- subdivision of the element into n_{tetra} tetrahedra (triangles in 2D)
- initialization of counter ct at n_{tetra}
- loop on the n_F discontinuities
  - loop on the n_{tetra} tetrahedra
    - subdivision of i_{tetra} into $n_{sub-tetra}$ sub-tetrahedra
      - the connectivity of the first sub-tetrahedron overwrites that of i_{tetra}
    - loop on the $(n_{sub-tetra} - 1)$ last sub-tetrahedra
      - $ct = ct + 1$
      - the connectivity of $i_{sub-tetra}$ is written in position ct
  - n_{tetra} is updated to ct for the next discontinuity to take into account the new sub-tetrahedra

12 sub-elements to generate three areas. A possible improvement would be to integrate on each area with Lassere's method [20] that was adapted to X-FEM in [27].

3.3 Junction and multiple branched discontinuities

In the case of branched discontinuities, multi-Heaviside enrichment and multi-cutting are activated. The model is enriched with the junction function of [8]. The approach is illustrated in Fig. 6. Considering a discontinuity F_2 that branches to F_1, a node is enriched by an Heaviside d.o.f. for F_2 if the part of its support on the side of F_1 where F_2 lies is totally cut by F_2. An arbitrary reference point $\mathbf{X}_{ref_2}$ situated on this side is sufficient to represent it. Then, the Heaviside

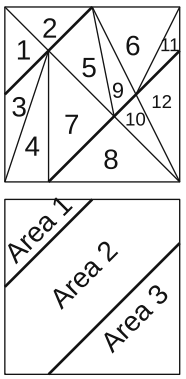

Area	Heaviside function	sub element
1	$+1, +1$	1,2
2	$-1, +1$	3,4,5,6 7,9,11
3	$-1, -1$	8,10,12

Fig. 5 Area cutting: each area contains sub-elements sharing the same Heaviside function value

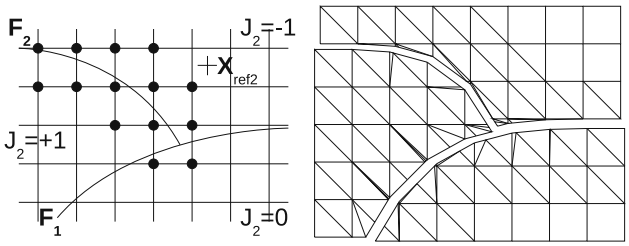

Fig. 6 Junction function J_2 and enriched nodes (*left*) and, possible deformed mesh of elements and subelements (*right*)

d.o.f. corresponding to F_2 are associated to a truncated generalized Heaviside function. The value is ± 1 and -1 on the side of F_1 where F_2 lies, and zero on the other side. A simple way to write the displacement approximation is to replace in Eq. (10), the term $H(\psi_{n_F}(\mathbf{X}))$ for $F = 2$ by:

$$J_2(\mathbf{X}) = \begin{cases} H(\psi_{n_2}(\mathbf{X})) \\ \quad \text{if } H(\psi_{n_1}(\mathbf{X}_{ref_2}))H(\psi_{n_1}(\mathbf{X})) > 0 \\ 0 \quad \text{else.} \end{cases} \tag{11}$$

An important difference from the multi-Heaviside approach of Sect. 3.1 is the dependency of J_2 on ψ_{n_1}, and not only on ψ_{n_2}. One can notice that ψ_{n_1} is already used to define F_1. Only a reference point is then needed to branch a discontinuity onto another one.

In the approach for multiple branches of [8], the strategy allowed to branch several secondary discontinuities on a main one but the case of a discontinuity which can be both principal and secondary was not discussed. We consider this case in Fig. 7, where a third discontinuity F_3 that branches to F_2 is introduced, F_2 branching to F_1. The term $H(\psi_{n_F}(\mathbf{X}))$ for $F = 3$ in Eq. (10) is replaced by:

$$J_3(\mathbf{X}) = \begin{cases} H(\psi_{n_3}(\mathbf{X})) \quad \text{if } \forall i \in \{1, 2\}, \\ \quad H(\psi_{n_i}(\mathbf{X}_{ref_3}))H(\psi_{n_i}(\mathbf{X})) > 0 \\ 0 \quad \text{else.} \end{cases} \tag{12}$$

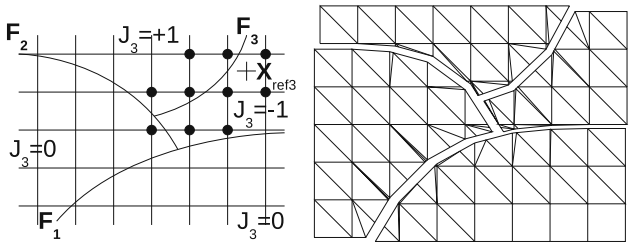

Fig. 7 Junction function J_3, enriched nodes (*left*) and possible deformed mesh of elements and subelements (*right*). Meshes on the *right* show elements as well as sub-elements used for integration but not contributing to new d.o.f.

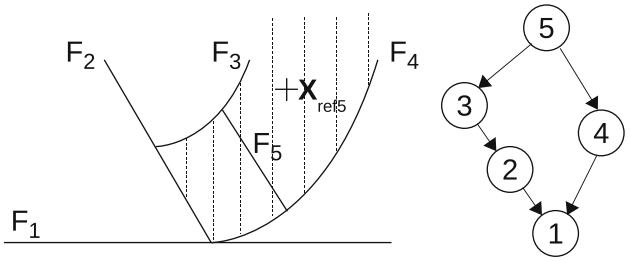

Fig. 8 Discontinuity network example (*left*) and corresponding hierarchical tree (*right*). The *shaded* area corresponds to the domain where the enrichment function for discontinuity 5 is non zero

To avoid ambiguities in the area where J_2 is equal to zero, we decided to set also J_3 to zero in this area. The level set ψ_{n_1} is needed to determine this area. Then, one can notice in Eq. (12) the dependency on ψ_{n_3} and ψ_{n_2}, but also on the previous level set ψ_{n_1}, while F_3 is not directly connected to F_1. For a more complex network (Fig. 8 for example), a hierarchical tree is built to take into account the connectivity of the branched discontinuities. Let S_F be the set of the previous branched discontinuities for F and $\mathbf{X}_{ref_F}$ a reference point for discontinuity F, the enrichment function to be added reads:

$$J_F(\mathbf{X}) = \begin{cases} H(\psi_{n_F}(\mathbf{X})) & \text{if } \forall i \in S_F, \\ \quad H(\psi_{n_i}(\mathbf{X}_{ref_F}))H(\psi_{n_i}(\mathbf{X})) > 0 \\ 0 \quad \text{else.} \end{cases} \tag{13}$$

In the example of Fig. 8, the set of the previous connected discontinuities for F_5 is $S_5 = \{1, 2, 3, 4\}$. Then, Eq. (13) gives the shaded area where the enrichment function for F_5 is non zero.

4 Contact and junction

In this section, the junction approach is extended to contact conditions. The variational form of contact with an augmented Lagrangian was detailed in Sect. 2. The difficulty with X-FEM is to approximate the contact pressure over a LBB stable space. Shape functions that are used in classical FEM are associated to the contact facets through their nodal values (see Fig. 9 on the left). With X-FEM, we follow the interpolation proposed by [4]. The contact pressure is still evaluated on the facets, but the nodal values are associated with the bulk element shape functions (see Fig. 9 on the right). For the LBB condition, a reduction is performed by the algorithm of [17] that selects a minimal space of cut edges, called vital. The number of Lagrange d.o.f. is reduced to the number of vital edges. To associate one contact d.o.f. to each vital edge, the Lagrange multipliers of the two nodes are linked by an equality relation as proposed by [4] (see Fig. 9 on the right). Extension to 3D, and special treatment for quadrangles and hexahedra is detailed in [35].

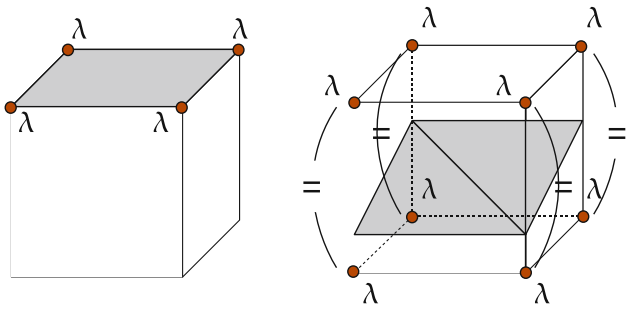

Fig. 9 Contact facets (*shaded* areas) and contact unknowns: FEM (*left*), X-FEM (*right*). On the *right* side, the Lagrange multipliers of the two nodes of each vital edge are linked by an equality relation

4.1 Multiple enrichment and contact formulation

The method, which was originally built for an enrichment with a single discontinuity is generalized here to the case of multiple enrichments. By exploiting the data structure used for the multiple enrichment (see Sect. 3.1), the extension to multiple enrichments is then simple. A node is enriched by the same number of Lagrange multipliers than its number of Heaviside d.o.f. Each Lagrange multiplier is associated to a Heaviside one, with the same numbering for simplicity.

A simple example is illustrated in Fig. 10 where a stair-step pressure is applied to introduce sliding. The mesh is composed of 4 cells, so that each cell is cut twice. The support of the nodes at $Y = 2$ are cut 4 times and then, these nodes hold the d.o.f. ($\mathbf{a}$, $\mathbf{b}_1$, $\mathbf{b}_2$, $\mathbf{b}_3$, $\mathbf{b}_4$, λ_1, λ_2, λ_3, λ_4). As for the example presented in Fig. 9, each pair of Lagrange multipliers associated to a vital edge is linked by an equality relation.

4.2 Contact over the junction

The generalization of contact to elements containing a junction is more complex. To simplify, in this section we will assume small sliding.

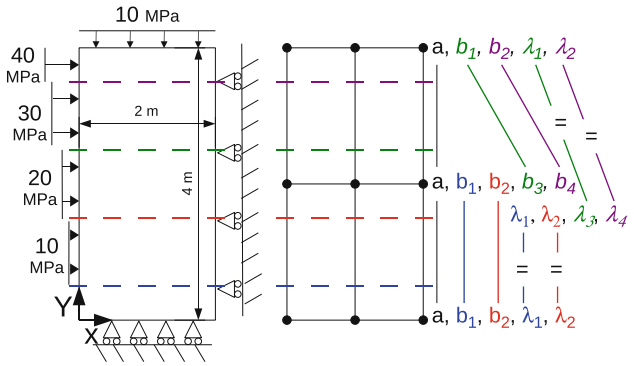

Fig. 10 *Rectangle* totally cut by four interfaces: data for the contact problem (*left*), mesh and enrichment (*right*)

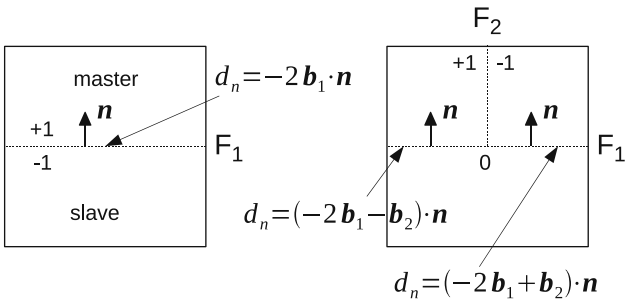

Fig. 11 Displacement jump in the case of one enrichment (*left*) and with the introduction of a junction enrichment (*right*)

The computation of the contact displacement jump d_n is represented for the case of a single enrichment in the left part of Fig. 11. The Heaviside function is $+1$ on the master side and -1 on the slave side. Along the lines of [17], by choosing arbitrarily the top surface as the master side, the normal distance between a slave point and its projection given by Eq. (2) reduces, with the help of Eq. (8), to:

$$d_n = \mathbf{n} \cdot \sum_{j \in J} (-2)\mathbf{b}_j \phi_j(\mathbf{X}). \tag{14}$$

With the junction enrichment, the Heaviside function associated with the discontinuity that generates the facet (see Fig. 9) is not sufficient to compute d_n and this simplification is no longer available. From Eqs. (10) and (13) (using the same notations), the displacement jump is more complex and reads:

$$d_n = \mathbf{n} \cdot \sum_{j \in J} \phi_j(\mathbf{X}) \sum_{i_H=1}^{n_H} \mathbf{b}_{i_H,j} \Delta H_{i_H,j}, \tag{15}$$

with the jump of the enrichment function:

$$\Delta H_{i_H,j} = \begin{cases} J_{F(i_H,j)}(\mathbf{x}^1) - J_{F(i_H,j)}(\bar{\mathbf{x}}^1) \\ \text{if } F \text{ is a junction,} \\ H\big(\psi_{n_F(i_H,j)}(\mathbf{x}^1)\big) - H\big(\psi_{n_F(i_H,j)}(\bar{\mathbf{x}}^1)\big) \\ \text{else.} \end{cases} \tag{16}$$

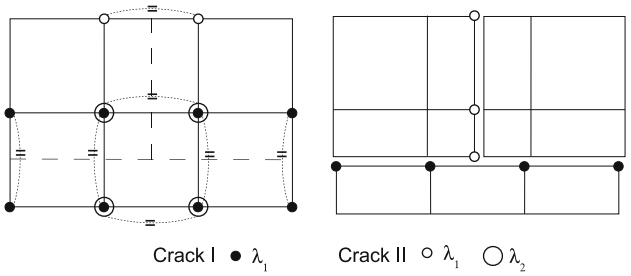

Fig. 12 Introduction of contact d.o.f. into a junction: for the X-FEM model (*left*) with equality relations imposed by the LBB algorithm and for the kinematically equivalent FEM model (*right*)

Table 1 Number of d.o.f. per type for a junction with XFEM and FEM

Discrete scheme	**a**	**b** (crack I)	**b** (crack II)	λ (crack I)	λ(crack II)
X-FEM	12	8	6	$8-4=4$	$6-3=3$
FEM	26			4	3

An illustration is given in the right part of Fig. 11, where the jump over F_1 depends also on the d.o.f. associated to the Heaviside function related to F_2.

We now check that our X-FEM version of contact is equivalent to its FEM counterpart. Figure 12 compares the contact d.o.f. discrete space of X-FEM at left, with that of FEM at right, for the junction of a vertical crack II with a horizontal crack I. Assuming 1D kinematics to simplify, the number of d.o.f. is indicated in Table 1. Note that for the FEM model, the slave surface is arbitrarily chosen as the bottom surface for crack I and as the left surface for crack II. For the X-FEM model, some nodes hold two distinct Lagrange multipliers (one for each crack). A large circle is then used for crack II to mark the distinction in Fig. 12. The total number of displacement d.o.f. is 26 and the total number of contact d.o.f. is 7, both for the FEM and the X-FEM case, showing that the discrete spaces of both formulations are equivalent.

Let us now detail the discrete interpolation of the contact reaction on both cracks. Obviously, in case of linear bulk elements, a natural choice is to use linear $P1$ interpolation for contact reactions inside the elements which do not contain the junction. In the junction elements, the interpolation scheme is constrained by the maximum number of available contact d.o.f. (see Table 1). The element containing the junction has two independent contact d.o.f. for each crack. A first simplified version is proposed as represented in the left part of Fig. 13, with a $P0$ constant interpolation only on crack II. The contact reaction on the part of crack I which is inside the junction element is disregarded (assumed to be zero). A second version is shown in the center part of Fig. 13. It improves the representation of contact with a $P0$ interpolation on crack II and on both cut parts of crack I. This version uses three contact d.o.f. A third version finally uses the fourth available

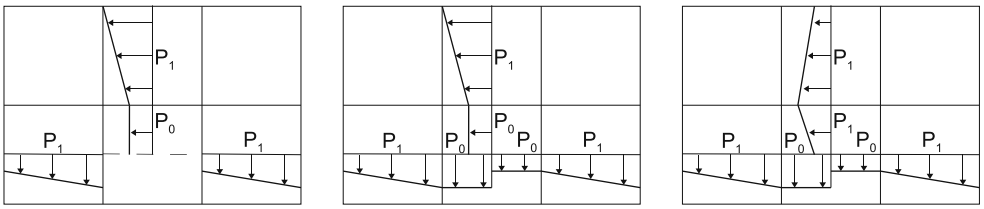

Fig. 13 Interpolation choice for the junction: $nothing$–$P0$ (*left*), $P0$–$P0$ (*center*) and $P0$–$P1$ (*right*)

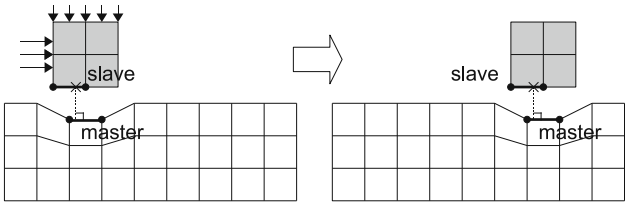

Fig. 14 Pairing example in FEM: the contact element changed in between the initial state (*left*) and the final state (*right*)

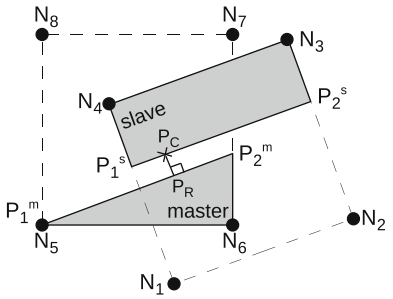

Fig. 15 Contact element with X-FEM

d.o.f. to obtain a $P1$ interpolation of the contact reaction profile along the crack II, as shown in the right part of Fig. 13. In the following of this paper, the $P0$–$P0$ and $P0$–$P1$ versions will be employed only in simplified problems. For more complex problems, the $nothing$–$P0$ choice is used because we lack a general algorithm to cut the discontinuity surfaces in the junction elements, which is needed for the numerical contact integration.

4.3 Large sliding

We are now interested in the spatial discretization of the variational form of the equilibrium given by Eq. (6) and of the variational form of the contact conditions given by Eq. (7). In a classical master–slave FEM strategy, two surface elements are associated after the projection of a slave point of the slave element on the master surface. A contact element is then built from the union of the slave and of the master surface elements, see Fig. 14.

The X-FEM case differs because of the absence of elements representing the surfaces in contact. We follow here the strategy given by [29] for a single discontinuity. A discretized slave surface is first built by joining the points of intersection of the iso-zero of the normal level set function with the bulk X-FEM elements. When the locations of the intersection points is updated after adding the total displacement (including its discontinuous part) to the initial position, it is possible to know the current location of any point belonging to the initial slave surface. It is then possible to project it on a similarly built master surface. The key idea in [29] is then to build a contact element resulting from the union of two bulk X-FEM elements, one corresponding to the slave surface and the other one associated to the master surface (see Fig. 15). This idea has been extended here to the case of multiple discontinuities with the enrichment described in Sect. 3.1 and with the corresponding kinematic and contact d.o.f., see Sect. 4.1. The list of d.o.f. depending on the enrichment is given for the slave part and for the master part in Table 2.

Table 2 X-FEM element types

Element	Kinematic d.o.f.			Contact d.o.f.	
H_1					
m	$\mathbf{a}$	$\mathbf{b}_1$			
s	$\mathbf{a}$	$\mathbf{b}_1$		λ_1	
H_2					
m	$\mathbf{a}$	$\mathbf{b}_1$	$\mathbf{b}_2$		
s	$\mathbf{a}$	$\mathbf{b}_1$	$\mathbf{b}_2$	λ_1	λ_2
H_3					
m	$\mathbf{a}$		$\mathbf{b}_{1,2,3}$		
s	$\mathbf{a}$		$\mathbf{b}_{1,2,3}$		$\lambda_{1,2,3}$
H_4					
m	$\mathbf{a}$		$\mathbf{b}_{1,2,3,4}$		
s	$\mathbf{a}$		$\mathbf{b}_{1,2,3,4}$		$\lambda_{1,2,3,4}$
H_1F					
m	$\mathbf{a}$	$\mathbf{b}_1$	$\mathbf{c}_1$		
s	$\mathbf{a}$	$\mathbf{b}_1$	$\mathbf{c}_1$	λ_1	
F	$\mathbf{a}$	$\mathbf{c}_1$		λ_1	

Limiting the maximum number of discontinuities to four for practical purposes, the list of contact element types is:

- H_i–H_j with $i \in [1,4]$ and $j \in [1,4]$,
- H_1–H_1F and H_1F–H_1,
- H_1F–H_1F,

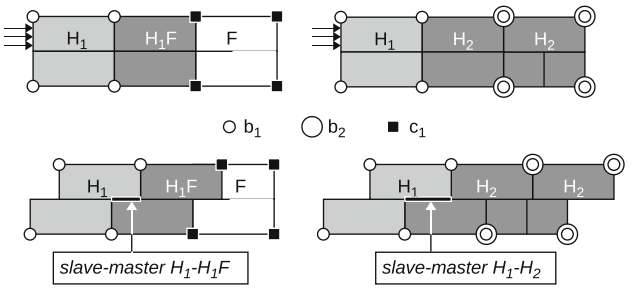

Fig. 16 Pairing examples between different X-FEM elements. Element H_1–H_1F for a crack front (*left*), element H_1–H_2 for a junction (*right*)

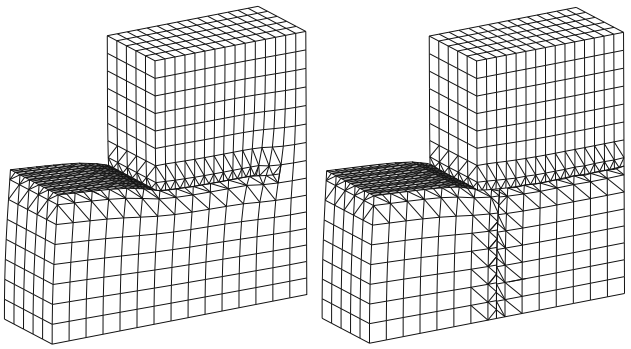

Fig. 17 Application examples of contact with large sliding, using contact element H_1–H_1F for a crack front (*left*), and H_1–H_2 for a junction (*right*)

as illustrated in Table 2 when each element type is described. Note that the case of a F–F contact element has been disregarded because small sliding can be assumed in this area, as is shown in the lower left part of Fig. 16.

For the sake of illustration, Fig. 17 shows an example of an X-FEM simulation with large sliding for a single discontinuity (left) and with a junction (right).

5 Matrix conditioning

The condition number, denoted $K = 10^{\delta}$, corresponds to the ratio of the biggest to the smallest eigenvalue of the matrix. For a computation in double precision, with a numerical error of about 10^{-15}, the relative error will be of about $10^{-15+\delta}$. For example, we should guarantee $\delta < 10$ to get a numerical error less than 10^{-5}. Straightforward use of geometrical enrichment for crack-tips leads to ill-conditioned matrices [3,19]. To improve the global condition number, [3] propose to orthogonalize locally the stiffness matrices. Ill-conditioning is justified in [19] by the fact that the chosen functions F_α in Eq. (8) do not form locally a free basis of function. A global enrichment is proposed in [19] to solve the problem. However, these solutions do not prevent system ill-conditioning, especially with the use of quadratic elements [19].

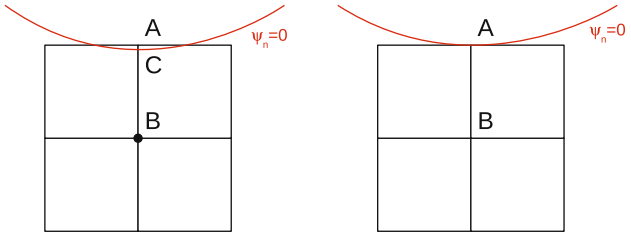

Fig. 18 Fit to vertex principle. If the discontinuity is too near to node A (*left*), we adjust the discontinuity to go through node A (*right*) by setting the level set value at node A to zero

Ill-conditioning also comes from the Heaviside enrichment, when the crack is located close to a node. We describe in the following sections some technical solutions to solve this problem in case of junctions.

5.1 Fit to vertex

The fit to vertex [24] is a simple procedure that consists to set the value $\psi_n = 0$ for a node located very near to the crack surface. A linear criterion based on an edge lengths ratio is used as illustrated in Fig. 18. On the left, the Heaviside d.o.f. associated to point B leads to ill-conditioning. On the right, we assume the linear criterion $\frac{AC}{AB} < 10^{-\gamma}$ to be satisfied. The crack is then fitted to point A by setting the level set value at node A to zero and B is not enriched.

The value γ can be analytically related to δ (see Fig. 19) by computing the stiffness matrix of a reference element that is cut in configurations where the fit to vertex is borderline to be activated. The maximum condition number can then be predicted for these configurations. The fit to vertex, usually realized at 1 % of the edge length ($\gamma = 2$), should be used when ill-conditioning increases but cannot be set to a larger value (>1 % or $\gamma < 2$) in order to avoid unrealistic changes of the crack geometry. For the example of quadratic hexahedron, the fit to vertex should be set to more than 10 % of the edge length if one expects a maximum condition number of about 10^{10}, which is not acceptable practically.

The case of junctions is more complicated as shown on the left of Fig. 20. In this example, the small gray volume generated by the second crack leads to ill-conditioning but the fit to vertex cannot filter out its Heaviside d.o.f. To solve this problem, a relative tolerance on the distance between the intersection points generated by the discontinuities over the edges during the introduction of multiple cracks is used. On the right of Fig. 20, the introduction of the second crack generates a new intersection point. If the distance between both intersection points is lower than a given criterion, then the new intersection point is not added as illustrated by the right part of Fig. 20. The gray volume is then automatically set to zero and the node is not enriched for the second crack. In addition, this linear criterion is useful to avoid to generate too small

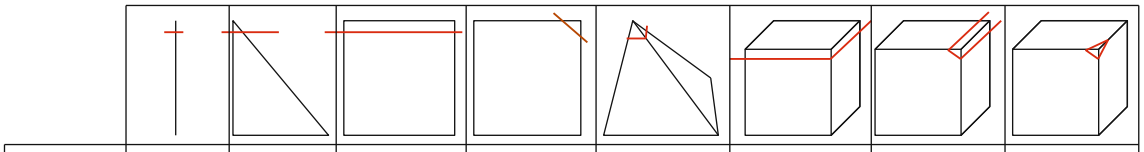

linear	$\delta = \gamma$	$\delta = 2\gamma$	$\delta = \gamma$	$\delta = 4\gamma$	$\delta = 3\gamma$	$\delta = \gamma$	$\delta = 4\gamma$	$\delta = 7\gamma$
quadratic	$\delta = 3\gamma$	$\delta = 4\gamma$	$\delta = 3\gamma$	$\delta = 6\gamma$	$\delta = 5\gamma$	$\delta = 3\gamma$	$\delta = 6\gamma$	$\delta = 9\gamma$

Fig. 19 Value of δ as a function of γ for 1D, 2D and 3D cut elements. The first *line* is obtained in the case of linear shape functions and the second one in the case of quadratic shape functions (i.e. conditioning of 10^{δ})

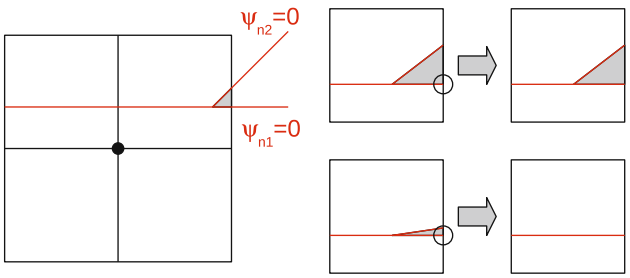

Fig. 20 Example where the area associated with the support of a nodal shape function is very small and cannot be corrected by the fit to vertex (*left*) and tolerance on the intersection points distance to solve the problem (*right*)

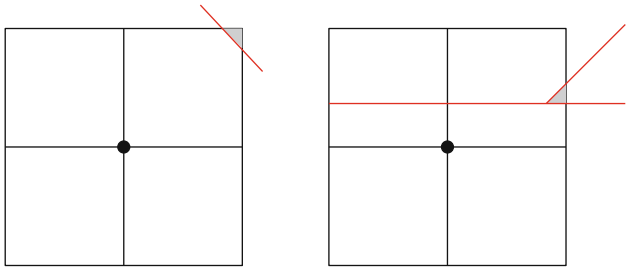

Fig. 21 Volumetric criterion evaluation: the *gray* volume is compared to the total support of the nodal shape function. Case without junction (*left*) and with junction (*right*)

sub-elements during the sequential cutting (see Sect. 3.2). To expect correct results in practice, the distance is set to 10^{-6} times the characteristic length of the element. If we refer to Fig. 19, this corresponds to $\gamma = 6$ and leads to ill-conditioning for all 2D and 3D elements, even for 2D linear ones.

5.2 Volumetric criterion

The volumetric criterion proposed by [8] is more adapted to the case of a junction. It consists in comparing for each support of a node that is supposed to be enriched by an Heaviside d.o.f., the ratio of areas on both sides of the crack affected by the Heaviside value ± 1 with respect to the total area. The criterion reads:

$$\frac{\min(V_{-1}, V_1)}{V} \leq 10^{-\alpha}, \tag{17}$$

where V is the total volume of the support of the node, and V_{-1}, V_1 are the volumes where the Heaviside function is ± 1 with α as a parameter. The value $\alpha = 4$ is typically used. If a node verifies the criterion, its Heaviside d.o.f. is eliminated by setting it to zero. Two examples are given in Fig. 21 to illustrate the procedure.

This criterion is relevant for linear elements (triangle, tetrahedron), but not for multi-linear elements (quadrangle, pyramid, pentahedron, hexahedron) and quadratic elements. Indeed $\alpha = 4$ induces eliminating some d.o.f. and that perturbs the kinematic approximation and the solution of the problem, whereas greater values of α deteriorate the condition number. To take that into account, we propose a similar but more precise criterion based on the evaluation of stiffness ratios. In the two examples given in Fig. 21, we now evaluate the ratio of the stiffness of the gray area compared to the total stiffness associated to the node. This new criterion reads:

$$\frac{\min(\int_{\Omega_{-1}} \|\phi_{,\mathbf{X}}\|^2 d\Omega, \int_{\Omega_1} \|\phi_{,\mathbf{X}}\|^2 d\Omega)}{\int_{\Omega} \|\phi_{,\mathbf{X}}\|^2 d\Omega} \leq 10^{-\delta}, \tag{18}$$

where Ω is the support of the node, Ω_{-1}, Ω_1 are the parts of the support where the Heaviside function is ± 1, $\phi_{,\mathbf{X}}$ is the derivative of the shape function associated to the node in the global coordinate basis $\mathbf{X}$ and δ is a parameter directly related to the expected maximum condition number. This parameter is typically chosen between 8 and 10, that leads to a maximum condition number close to 10^{δ}. This criterion is based on a relative stiffness that allows to disregard the material behavior which can be eliminated as it appears both to the numerator and discriminator of the ratio. It is then possible to discriminate a priori, as for the volumetric criterion, the d.o.f. that should be set to zero. The norms in Eq. (18) mean that we consider the criterion in all the directions of the space, but it is also possible to consider the directions individually. Note that for linear elements, $\phi_{,\mathbf{X}}$ is quasi-constant and the stiffness criterion is then equivalent to the volumetric criterion.

We present an example in Fig. 22, which allows to compare the error generated by the elimination with the

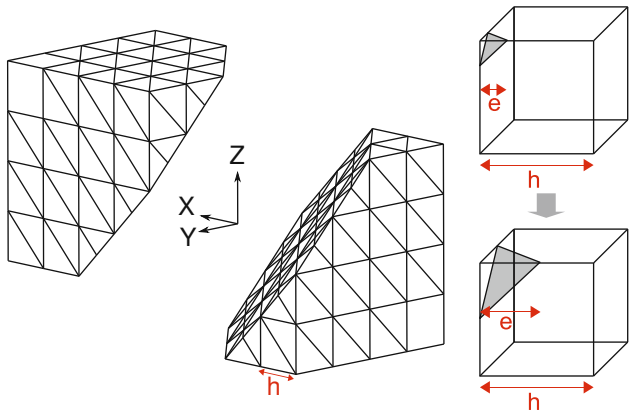

Fig. 22 Displacement for the level set function $X+Y+Z+e=0$ with $e=0$ (*left*) and evolution of the interface for a *hexahedron cut* in its corner as e increases (*right*)

volumetric and stiffness criteria. A cube meshed with 64 hexahedra is completely cut by an interface with the level set function $X+Y+Z+e=0$ and submitted to an opening mode without strain (see Fig. 22 on the left). The test consists in changing the level set function by moving the parameter e from zero to $\frac{h}{2}$ where h is the element length. Some hexahedra become cut in their corners (see Fig. 22 on the right), generating small tetrahedra responsible for ill-conditioning. The condition number is numerically evaluated in terms of the small tetrahedron volume, characterized by the aspect ratio e/h. The results are given in Fig. 24. The relative error of the displacement on the interface is also given in Fig. 25. Without any criterion, the fit to vertex gives a good conditioning for $\frac{e}{h} \leq 0.01$. The hexahedron cut in its corner being the worst configuration in Fig. 19, the same conclusion can be expected for other elements in other configurations. When the fit to vertex ceases, a peak of ill-conditioning is responsible for an important error in the displacement. Then, the condition number and the error decrease when $\frac{e}{h}$ increases. With the eliminations, the condition number is improved, but some errors related to the elimination process appear on the solution. Finally, a better condition number and errors are obtained for the stiffness criterion than for the volumetric one.

To evaluate the influence of the error generated by the elimination, we take up the case presented in Fig. 22. The test is still done in opening mode, but an homogeneous compression is applied on the two blocks of the structure to evaluate the energy error when refining the mesh. The stiffness criterion is used for the elimination and the ratio $\frac{e}{h}$ is fixed to 0.022. This value gives the worst relative error for this criterion. The results are given in Fig. 23. The conclusions of this patch test is that first, the error on the displacement observed in Fig. 25 leads to a similar energy error, while the latter should be numerically zero. Secondly, the energy error does not decrease when the mesh is refined, while the ratio of nodes where a d.o.f. is eliminated in comparison to the total number of nodes decreases.

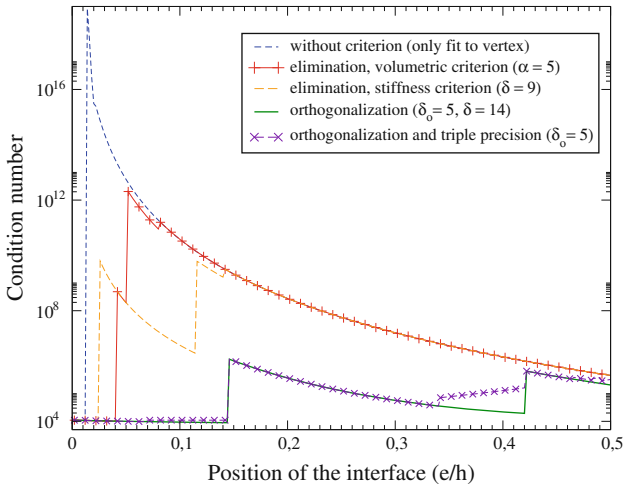

Fig. 23 Condition number

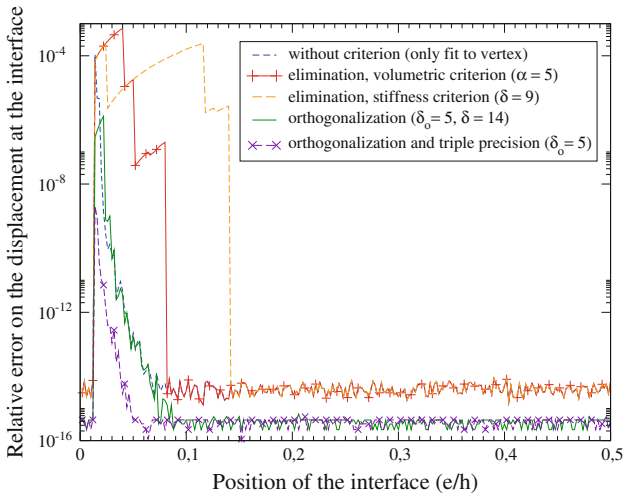

Fig. 24 Error on the displacement

5.3 Orthogonalization

The solution proposed here consists of replacing the elimination of the Heaviside d.o.f. by an orthogonalization of the local stiffness matrix, which is based on the X-FEM preconditioning of [3]. We suppose the system $\mathbf{Ku}=\mathbf{f}$ to be solved. $\mathbf{K}$ contains a local ill-conditioned sub matrix $\mathbf{A}$ (supposed to be symmetric), associated in our case to a node enriched by an Heaviside d.o.f. with support Ω:

$$\mathbf{K} = \begin{bmatrix} \ddots & \vdots & \\ & \mathbf{A} & \cdots \\ & & \ddots \end{bmatrix} \qquad (19)$$

$$\text{with } \mathbf{A} = \begin{bmatrix} \int_\Omega \phi_{,\mathbf{X}} \mathbf{C} \phi_{,\mathbf{X}} d\Omega & \int_\Omega \phi_{,\mathbf{X}} \mathbf{C} \phi_{,\mathbf{X}} H d\Omega \\ sym & \int_\Omega \phi_{,\mathbf{X}} \mathbf{C} \phi_{,\mathbf{X}} d\Omega \end{bmatrix}$$

where $\mathbf{C}$ is the Hooke tensor. $\mathbf{K}$ is then ill-conditioned because of $\mathbf{A}$. The principle is to use a Cholesky decomposition of the local matrix $\mathbf{A}$, $\mathbf{A} = \mathbf{G}\mathbf{G}^T$ and then, to use this decomposition to change the terms associated to this node in the global system:

$$\begin{array}{l} \tilde{\mathbf{K}} = \mathbf{R}\mathbf{K}\mathbf{R}^T \\ \tilde{\mathbf{f}} = \mathbf{R}\mathbf{f} \\ \tilde{\mathbf{K}}\tilde{\mathbf{u}} = \tilde{\mathbf{f}} \\ \mathbf{u} = \mathbf{R}^T\tilde{\mathbf{u}} \end{array} \quad \text{with} \quad \mathbf{R} = \begin{bmatrix} \mathbb{I} & \mathbf{0} & \mathbf{0} \\ \mathbf{0} & \mathbf{G}^{-1} & \mathbf{0} \\ \mathbf{0} & \mathbf{0} & \mathbb{I} \end{bmatrix}, \tag{20}$$

A good conditioning is then obtained for $\tilde{\mathbf{K}}$.

In our implementation, this procedure is simplified. First, the orthogonalization is only done for a node where a Heaviside d.o.f. satisfies a certain value of the stiffness ratio given by the left hand side of Eq. (18). This ratio is denoted ϵ. Secondly, it is not mandatory to use the exact local matrix for the Cholesky decomposition: a simplified matrix is used. As for Eq. (18), the simplified matrix is obtained in two steps. To have a dimensionless matrix, the material behavior is disregarded and the matrix is normalized:

$$\begin{aligned} \mathbf{A}_1 &= \frac{\begin{bmatrix} \int_\Omega \phi_{,\mathbf{X}}^2 d\Omega & \int_\Omega \phi_{,\mathbf{X}}^2 H d\Omega \\ sym & \int_\Omega \phi_{,\mathbf{X}}^2 d\Omega \end{bmatrix}}{\int_\Omega \|\phi_{,\mathbf{X}}\|^2 d\Omega} \\ &= \begin{bmatrix} \frac{\int_\Omega \phi_{,\mathbf{X}}^2 d\Omega}{\int_\Omega \|\phi_{,\mathbf{X}}\|^2 d\Omega} & \frac{\int_\Omega \phi_{,\mathbf{X}}^2 d\Omega - 2\int_{\Omega_{-1}} \phi_{,\mathbf{X}}^2 d\Omega}{\int_\Omega \|\phi_{,\mathbf{X}}\|^2 d\Omega} \\ sym & \frac{\int_\Omega \phi_{,\mathbf{X}}^2 d\Omega}{\int_\Omega \|\phi_{,\mathbf{X}}\|^2 d\Omega} \end{bmatrix}. \end{aligned} \tag{21}$$

Then, a normalized block matrix is employed:

$$\begin{aligned} \mathbf{A}_2 &= \begin{bmatrix} \frac{\int_\Omega \|\phi_{,\mathbf{X}}\|^2 d\Omega}{\int_\Omega \|\phi_{,\mathbf{X}}\|^2 d\Omega}\mathbb{I} & \frac{\int_\Omega \|\phi_{,\mathbf{X}}\|^2 d\Omega - 2\int_{\Omega_{-1}} \|\phi_{,\mathbf{X}}\|^2 d\Omega}{\int_\Omega \|\phi_{,\mathbf{X}}\|^2 d\Omega}\mathbb{I} \\ sym & \frac{\int_\Omega \|\phi_{,\mathbf{X}}\|^2 d\Omega}{\int_\Omega \|\phi_{,\mathbf{X}}\|^2 d\Omega}\mathbb{I} \end{bmatrix} \\ &= \begin{bmatrix} \mathbb{I} & \pm(1-2\epsilon)\mathbb{I} \\ sym & \mathbb{I} \end{bmatrix} \end{aligned} \tag{22}$$

to finally obtain at the zero order approximation:

$$\mathbf{G} = \begin{bmatrix} \mathbb{I} & 0 \\ \pm\mathbb{I} & 2\sqrt{\epsilon}\mathbb{I} \end{bmatrix} \text{ and } \mathbf{R} = \begin{bmatrix} \mathbb{I} & \mathbf{0} & & \mathbf{0} \\ \mathbf{0} & \begin{bmatrix} \mathbb{I} & 0 \\ \frac{\pm 1}{2\sqrt{\epsilon}}\mathbb{I} & \frac{1}{2\sqrt{\epsilon}}\mathbb{I} \end{bmatrix} & & \mathbf{0} \\ \mathbf{0} & \mathbf{0} & & \mathbb{I} \end{bmatrix}. \tag{23}$$

In 1D, the procedure leads to the matrix:

$$\begin{aligned} \tilde{\mathbf{K}} &= \begin{bmatrix} \ddots & \vdots & \\ & \mathbf{G}^{-1}\mathbf{A}\mathbf{G}^{-T} & \cdots \\ & & \ddots \end{bmatrix} \\ \text{with } \mathbf{G}^{-1}\mathbf{A}\mathbf{G}^{-T} &= \begin{bmatrix} 1 & \pm\sqrt{\epsilon} \\ sym & 1 \end{bmatrix} E \end{aligned} \tag{24}$$

where E is Young's modulus. Note that the condition number of $\mathbf{A}$ is $\frac{1-\epsilon}{\epsilon}$ and becomes $\frac{1+\sqrt{\epsilon}}{1-\sqrt{\epsilon}}$ for $\mathbf{G}^{-1}\mathbf{A}\mathbf{G}^{-T}$.

The decomposition is only ϵ ratio dependent and can thus be computed if necessary, at the same time as the stiffness criterion and only once even for non-linear problems. These simplifications allow to save CPU time. We propose to use the stiffness ratio on the example presented in Fig. 22 as follows:

$$\begin{cases} \epsilon > 10^{-\delta_o} & \text{nothing is done,} \\ 10^{-\delta_o} > \epsilon > 10^{-\delta} & \text{orthogonalization,} \\ \epsilon < 10^{-\delta} & \text{elimination.} \end{cases} \tag{25}$$

The results using $\delta_o = 5$ and $\delta = 14$ are plotted in Figs. 24 and 25. With this new procedure, the condition number is bounded by 10^6 and an iterative solver can be used without global preconditioning for this example. However, good conditioning does not guarantee good results, especially when ϵ is near 10^{-14} (the error curve with orthogonalization fits the one without criterion) and the elimination has to be reactivated for lower values of ϵ. This error comes from the numerical evaluation of the local matrix associated with the Heaviside d.o.f. This phenomenon can be understood in 1D. We denote $\mathbf{A}'$ the numerical evaluation of $\mathbf{A}$ in Eq. (19). Introducing the numerical error ϵ':

$$\begin{aligned} \mathbf{A}' &= \begin{bmatrix} 1 & \pm(1-2\epsilon)+\epsilon' \\ sym & 1 \end{bmatrix} E \\ \text{and } \mathbf{G}^{-1}\mathbf{A}'\mathbf{G}^{-T} &= \begin{bmatrix} 1 & \pm\sqrt{\epsilon} + \frac{\epsilon'}{2\sqrt{\epsilon}} \\ sym & 1 \pm \frac{\epsilon'}{2\epsilon} \end{bmatrix} E. \end{aligned} \tag{26}$$

Comparing Eq. (26) to Eq. (24), it appears that $\frac{\epsilon'}{2\epsilon} << 1$ needs to be satisfied. Noticing that ϵ' is about 10^{-15} in double precision, this condition is not satisfied for $\epsilon < 10^{-14}$.

The evaluation of $\mathbf{A}$ generates a loss of precision of about $\frac{1}{\epsilon}$ on $\mathbf{A}'$ that propagates on the orthogonalized matrix. A solution to this last difficulty is to estimate local matrices in triple precision before applying the orthogonalization. The orthogonalized matrix is then kept in double precision so that ϵ' is now about 10^{-23}. In practice we only used triple precision to evaluate the terms corresponding to the line and the column of the nodes where the orthogonalization criterion is triggered. The results, plotted in Figs. 24 and 25, show that the idea works. Orthogonalization is done with the criterion $\delta_o = 5$ and elimination is not needed anymore.

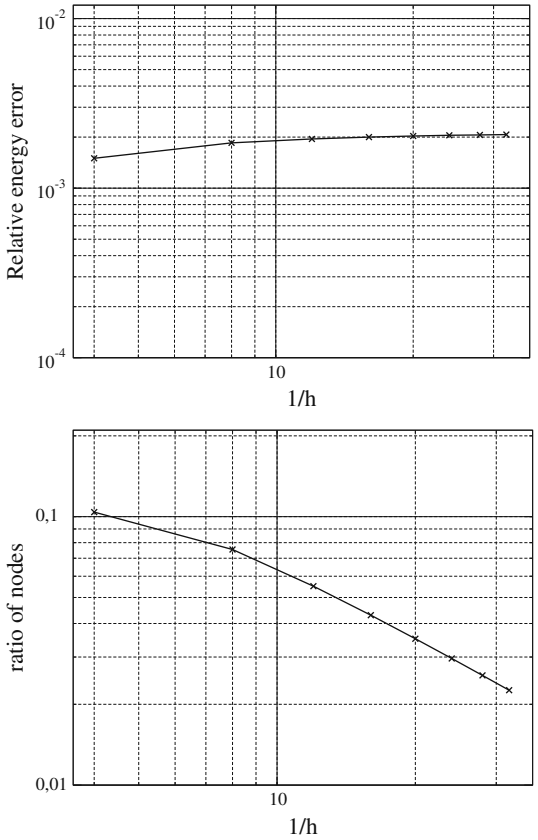

Fig. 25 Energy error (*top*) and ratio of nodes where a d.o.f. is eliminated in comparison to the total number of nodes (*bottom*)

6 Examples

6.1 Test of a frictionless block with a junction under compression

A 2D plane stress test is proposed to compare the 3 versions of the interpolation of the contact reaction in the elements containing a junction presented in Sect. 4.2. The domain is a square plate of 1m^2 area. Two discrete models are built with or without a junction and frictionless interfaces, see the right part of Fig. 26. Integration of the contact terms which come from the linearization of Eqs. (6) and (7) is performed with a 2 points Gauss quadrature.

Imposed boundary conditions are described in the left part of Fig. 26. The bottom surface is clamped. A parabolic profile of vertical pressure $p_y(X) = p_{max}(0.5 + 2X - 2X^2)$ is imposed on the top surface with p_{max} set to 1 MPa. Because the branching interfaces are frictionless, we choose to impose a horizontal profile of pressure on the lateral surfaces so that no bulk shear deformation is generated. Hence, this lateral pressure satisfies $p_x(Y) = 2p_{max}Y^2$. The modulus of elasticity is set to 10 GPa and for the sake of simplicity Poisson's ratio is set to zero. The resulting stress and strain tensors can be written in closed form expressions:

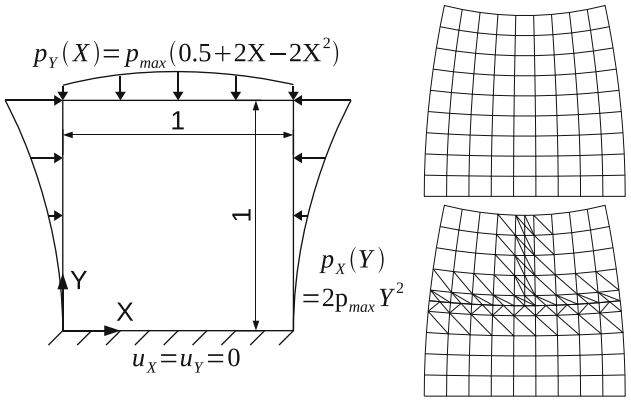

Fig. 26 Boundary value problem (*left*), deformation ($\times 1000$) without discontinuities and with two branched discontinuities and $P0$–$P1$ interpolation into the junction (*right*)

$$\begin{cases} \boldsymbol{\sigma}^{ref} = \begin{pmatrix} -p_X(Y) & 0 \\ 0 & -p_Y(X) \end{pmatrix} \\ \boldsymbol{\epsilon}^{ref} = \begin{pmatrix} -\frac{p_X(Y)}{E} & 0 \\ 0 & -\frac{p_Y(X)}{E} \end{pmatrix} \end{cases} \tag{27}$$

In Fig. 26, the right top part represents the deformation for the case without branching interfaces. The right bottom represents the deformation for the case with two branching interfaces and the $P0$–$P1$ interpolation of the contact reaction in the junction. The two solutions are qualitatively similar. We are now going to compare the convergence of the solutions when refining the mesh. In the following, an h superscript means that the quantity is computed with a mesh of characteristic size h. A ref superscript means that the quantity is computed for the reference closed form solution. The relative error in energy $W(\mathbf{u}^h)$ is defined as:

$$W(\mathbf{u}^h) = \sqrt{\frac{\int_\Omega \sigma(\nabla(\mathbf{u}^h - \mathbf{u}^{ref})) : \nabla(\mathbf{u}^h - \mathbf{u}^{ref}) d\Omega}{\int_\Omega \boldsymbol{\sigma}(\nabla \mathbf{u}^{ref}) : \nabla \mathbf{u}^{ref} d\Omega}}. \tag{28}$$

Figure 27 shows the convergence of $W(\mathbf{u}^h)$ for different configurations. The curve labels with fem correspond to the FEM solutions without the branching discontinuities. The other curves correspond to X-FEM solutions with the branching discontinuities for which the interpolation of the contact reaction in the junction element (see Sect. 4.2) is either $nothing$–$P0$, $P0$–$P0$ or $P0$–$P1$. As expected, the convergence is better for the $q4$ elements than for the $t3$ elements. Also, taking into account the contact reaction on the horizontal interface improves the convergence. A more remarkable result is that the convergence curves of all the studied cases have a unitary slope.

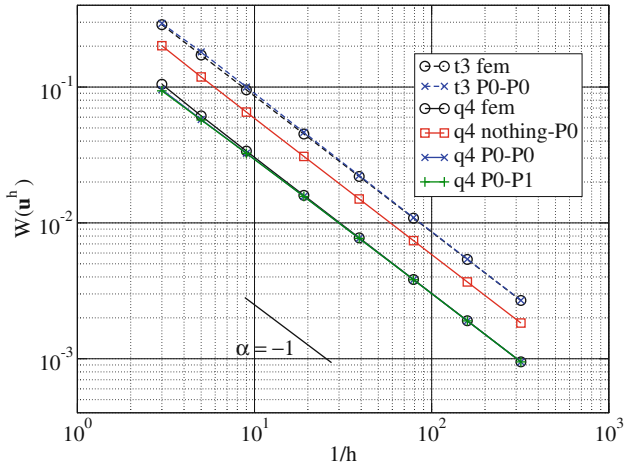

Fig. 27 Convergence error in $H^1(\Omega)$ norm: $t3$ indicates that the elements are linear triangles, while $q4$ indicates that the elements are bilinear quadrangles

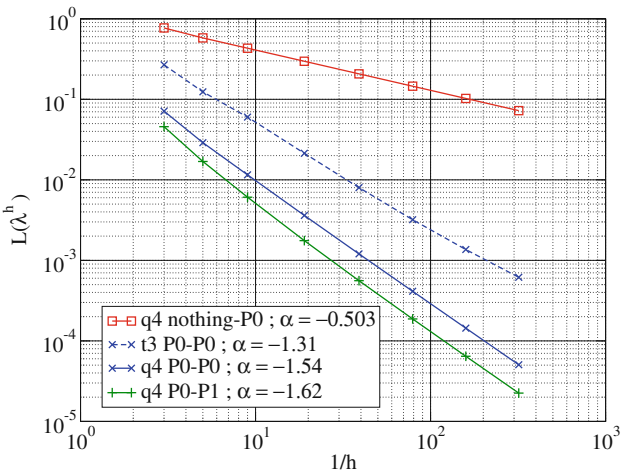

Fig. 28 Convergence error in the $L^2(\Gamma_c)$ norm for the contact pressure

To complete the comparison, we introduce the L^2 norm of the error in the contact reaction as:

$$L(\lambda^h) = \sqrt{\frac{\int\limits_{\Gamma_c} (\lambda^h - \mathbf{n}\cdot\sigma^{ref}\cdot\mathbf{n})^2 d\Gamma}{\int\limits_{\Gamma_c} (\mathbf{n}\cdot\sigma^{ref}\cdot\mathbf{n})^2 d\Gamma}}. \tag{29}$$

where $\mathbf{n}$ is the inward unit normal vector to the master interface. Figure 28 shows the convergence of $L(\lambda^h)$, for the X-FEM cases with frictionless interfaces. The absolute value of the convergence slope observed for the $P0$–$P0$ and $P0$–$P1$ cases in between 1 and 2 correspond to a theoretical super-linear convergence [38]. A striking difference with Fig. 27 is that the convergence rate for the $nothing$–$P0$ case is three times less than for the $P0$–$P0$ and $P0$–$P1$ cases. The error is also larger. This can be explained by the error completely taken into consideration in the junction region and underlines the importance of taking into account the contact contributions on all interfaces.

6.2 Stress intensity factors of closely interacting cracks

In this example we analyze the contact influence on a finite plate with multiple cracks. This example comes from a semi-analytic solution given by [41], and is also studied with X-FEM and harmonic enrichment in [28]. We consider the case where the plate size is 20 m × 20 m (see Fig. 29). Starting from an element size $h = 0.5$ m, we introduce cracks defined by points A to I and A' to I'. Coordinates are the same as those given in [41] or [28]. Then, the mesh is locally refined over the crack area and the crack front with five steps of adaptive mesh refinement according to a criterion function based on the distance to crack fronts. This function is computed by using level sets. The final mesh is composed of approximately 50,000 quadrangles and 5,000 triangles and the minimum mesh size value is $h = 0.015625$ m. A zoom on the crack area is given in the right part of Fig. 29.

We consider a homogeneous and isotropic material with Young's modulus $E = 10^5$ MPa and Poisson's ratio $\nu = 0.3$. Plane strain condition is assumed. A bitraction and shear load is applied by setting the following Neumann conditions on the plate boundary:

$$\mathbf{P} = \boldsymbol{\sigma}\cdot\mathbf{n} \quad \text{and} \quad \boldsymbol{\sigma} = \begin{pmatrix} 1 & 1 \\ 1 & 1 \end{pmatrix} \tag{30}$$

with $\mathbf{n}$ the outward normal to the boundary. Cracks are introduced into the structure using X-FEM (see Sect. 3). A topological enrichment is used for the crack fronts and the multi-Heaviside enrichment is used where junctions are activated. To compare the results with those given by [41] and [28], where traction-free condition on interior crack faces is assumed, we first perform a simulation without contact. The differences with a situation in which contact conditions are taken into account are then analyzed with a second simulation. The results are given in Fig. 30. An interpenetration area over the branched crack containing point C without contact is corrected with contact.

Computation of SIF has motivated many research works since the pioneering approach of [32] which proposed a path independent integral to compute the energy release rate. Taking advantage of the Maxwell–Betti reciprocal work theorem, the identification of mixed-mode singularities was then facilitated thanks to the interaction energy integral between the equilibrium solution and an auxiliary field [34]. More recently, FEM computation was simplified by replacing the contour integral by a domain formulation and the geometry were generalized to 3D cases [15]. In this paper, the SIF are computed with the theta method of [9], which stems from a Lagrangian derivation of the potential energy with respect

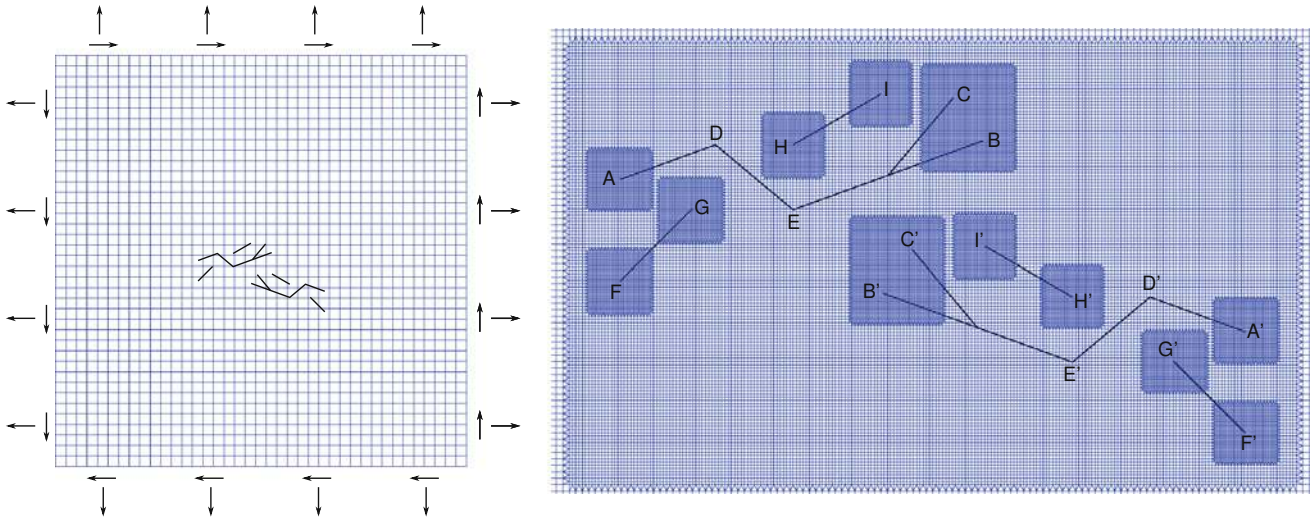

Fig. 29 Initial mesh and boundary condition (*left*), zoom on the crack area after five adaptive refinement steps (*right*)

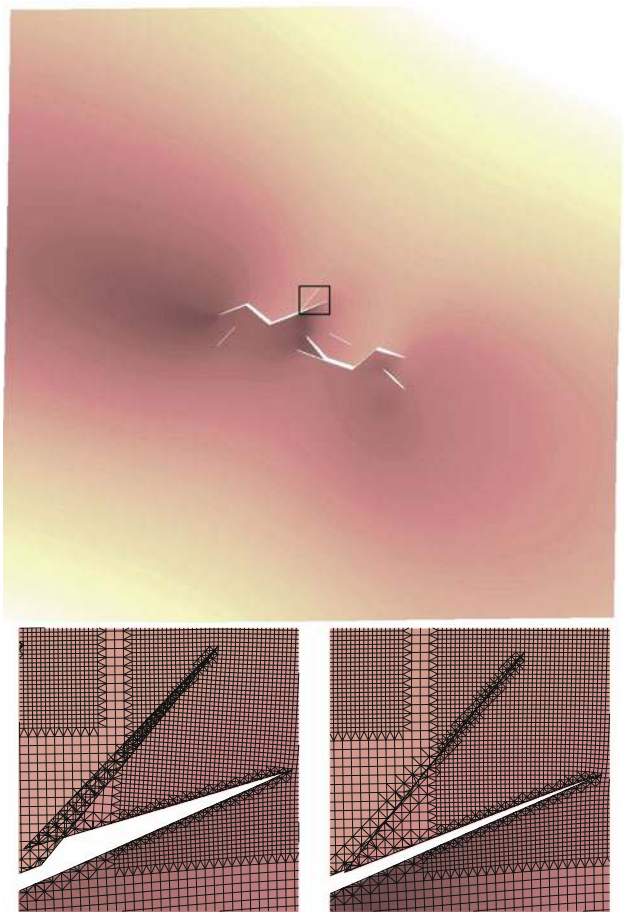

Fig. 30 Deformation with offset $\times 1000$ (*top*), zoom without and with contact (*bottom*). (Color figure online)

to the crack length when it reduces to zero and which leads to equivalent expressions than that of [15]. The results are presented in Table 3 for points A to I and Table 4 for points A' to I'. K^* corresponds to the reference given by [41]. K^H is the result obtained by [28] with the harmonic enrichment computed for quadratic elements with a subgrid 6×6 per element and a cartesian mesh composed of 84,375 quadrangles. K and K^c correspond to our results without and with contact respectively. Without contact, the calculated relative or absolute errors show that we recover the results given by the reference and that we reduce the errors with respect to [28] for a similar number of elements. With contact, the results for points A' to I' are unchanged because these cracks are in opening mode and the contact is not activated. For points A to I, we can notice two things. First, some negative K_I (for points C and G) are corrected when contact is added. Second, at the other points the values are strongly influenced by the global change of deformation when contact is taken into account.

To study the influence of this error in fatigue, we compute the propagation velocity at the crack tips with Paris's law. The direction of propagation is then given by the maximum hoop stress criterion [14] but similar results can be obtained with a criterion based on the minimum J local energy density [36] or on the energy release rate [30] for short cracks with small deviation angles. The norm of the velocity and the propagation angle are then given by:

$$\begin{aligned} &\|\mathbf{V}\| = \kappa . G^m \\ &\beta = 2 \arctan \tfrac{1}{4} \left(\tfrac{K_I}{K_{II}} - \text{sign}(K_{II}) \sqrt{\left(\tfrac{K_I}{K_{II}}\right)^2 + 8} \right), \end{aligned} \tag{31}$$

where (κ, m) are parameters which depend on the material behavior, usually determined experimentally and where G is the energy release rate. G is computed according to the theta method. We set $m = 3$, which corresponds to steel material. Eq. (31) depends linearly on κ. We are then free to set this

Table 3 SIF results in Pa$\sqrt{\text{m}}$ for points A to I

Points	A	B	C	F	G	H	I
K_I^*	1.7943	1.9932	−1.692	0.051	−0.5317	−0.0517	−0.1933
$\lvert\frac{K_I^H-K_I^*}{K_I^*}\rvert$ (%)	–	1.1	0.8	–	2.6	–	–
$\lvert\frac{K_I-K_I^*}{K_I^*}\rvert$ (%)	0.15	0.07	0.06	6.6	0.32	5.02	0.88
$\lvert\frac{K_I^c-K_I^*}{K_I^*}\rvert$ (%)	2.2	38.17	84.31	227.23	65.32	113.74	5.06
$\lvert K_I - K_I^*\rvert$	0.0027	0.0014	0.001	0.0034	0.0017	0.0026	0.0017
$\lvert K_I^c - K_I^*\rvert$	0.0395	0.7609	1.4265	0.1159	0.3473	0.0588	0.0098
K_{II}^*	2.8522	2.4042	−0.1337	0.2894	0.1885	−0.1979	0.0213
$\lvert\frac{K_{II}^H-K_{II}^*}{K_{II}^*}\rvert$ (%)	–	2.4	3.2	–	0.2	–	–
$\lvert\frac{K_{II}-K_{II}^*}{K_{II}^*}\rvert$ (%)	0.24	0.07	0.77	0.74	0.17	0.14	4.87
$\lvert\frac{K_{II}^c-K_{II}^*}{K_{II}^*}\rvert$ (%)	2.65	32.45	431.32	3.22	17.06	78.75	1086.23
$\lvert K_{II} - K_{II}^*\rvert$	0.0069	0.0016	0.001	0.0021	0.0003	0.0003	0.001
$\lvert K_{II}^c - K_{II}^*\rvert$	0.0756	0.7802	0.5767	0.0093	0.0322	0.1558	0.2314

Table 4 SIF results in Pa$\sqrt{\text{m}}$ for points A$'$ to I$'$

Points	A$'$	B$'$	C$'$	F$'$	G$'$	H$'$	I$'$
K_I^*	3.7215	2.67	5.3966	4.3255	3.6812	0.4157	1.0043
$\lvert\frac{K_I-K_I^*}{K_I^*}\rvert$ (%)	0.46	0.5	0.18	0.08	0.07	0.07	0.04
$\lvert\frac{K_I^c-K_I^*}{K_I^*}\rvert$(%)	0.21	0.04	0.5	0.05	0.1	5.05	3.18
$\lvert K_I - K_I^*\rvert$	0.0172	0.0133	0.0096	0.0035	0.0026	0.0003	0.0004
$\lvert K_I^c - K_I^*\rvert$	0.0077	0.0012	0.027	0.002	0.0038	0.021	0.0319
K_{II}^*	2.3379	1.0248	–0.1143	–0.1661	0.9279	–0.3947	0.0648
$\lvert\frac{K_{II}-K_{II}^*}{K_{II}^*}\rvert$ (%)	0.3	0.06	1.94	1.93	0.33	0.61	6.47
$\lvert\frac{K_{II}-K_{II}^*}{K_{II}^*}\rvert$ (%)	1.6	0.03	12.0	2.26	0.74	9.14	52.11
$\lvert K_{II} - K_{II}^*\rvert$	0.007	0.0006	0.0022	0.0032	0.003	0.0024	0.0042
$\lvert K_{II} - K_{II}^*\rvert$	0.0373	0.0003	0.0137	0.0038	0.0069	0.0361	0.0338

value since we are just interested in the deviation angle of propagation in this example.

Velocities are plotted in Fig. 31 with and without contact. We set velocities to zero when $K_I < 0$ to avoid non physical results for the angle β. Velocities for points A' to I' and point A are similar because the contact does not affect the SIF at these points. The relatively large deviations observed in Table 3 for points C, F, G, H, I is not visible in Fig. 31 because of the low SIF values for these points compared to the other points. Only the velocity at point B shows a significant difference when contact is taken into account. We notice that it is the only point in opening mode for which K_I and K_{II} values are modified if contact is taken into account, due to the corrected interpenetration over the branched crack containing point C (see Fig. 30).

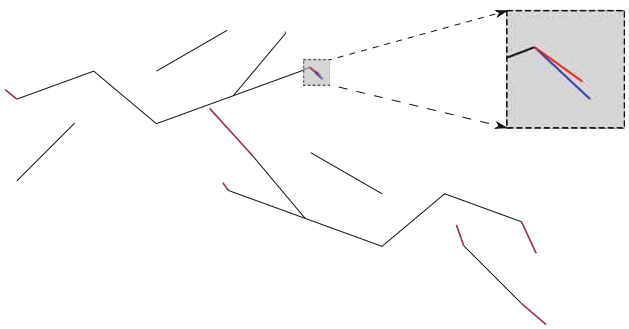

Fig. 31 Propagation directions with contact (*blue*) and without contact (*red*) for which the added segment lengths are linearly proportional to the norm of the velocity

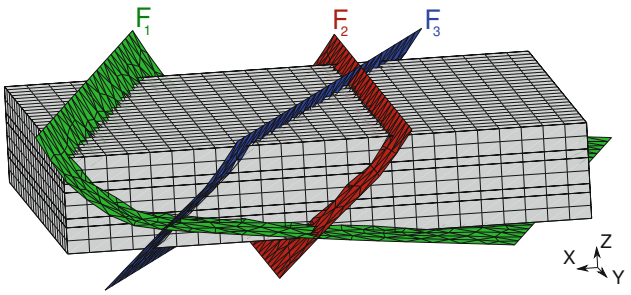

Fig. 32 Initial mesh of the basin with its three faults

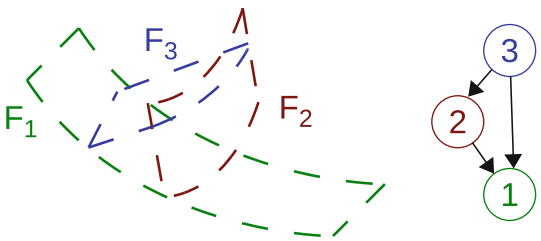

Fig. 33 Hierarchial tree of faults branching

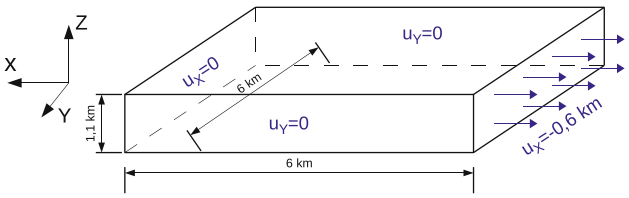

Fig. 34 Boundary conditions of the graben extension

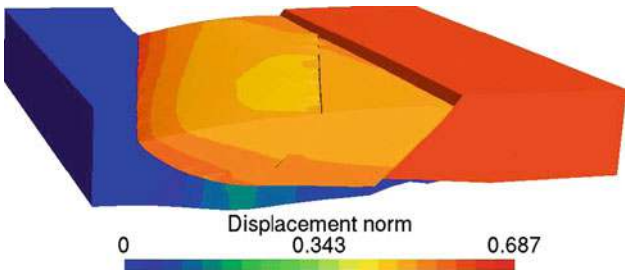

Fig. 35 Final state of the graben model. Isocontours represent the deformation

6.3 A 3D geological graben with branching faults

6.3.1 Problem settings

This final example illustrates the possibility of the presented X-FEM modeling of branched discontinuities to simulate a sedimentary basin deformation which is used in hydrocarbon exploration. Indeed, the design of a computational mesh which conforms to the fault surfaces remains difficult and generally requires a strong user interaction, see for examples [21] and [12]. The difficulty is mainly coming from the complexity of the branching patterns in 3D. X-FEM therefore provides an appealing alternative because it simplifies the design of geological models suitable to model the history of deformation of a basin.

The boundary value problem is shown in Fig. 32. At the initial stage, the basin is defined by a block of dimensions 6 km $\times$ 6 km $\times$ 1.1 km with a mesh composed of 4608 linear hexahedra. The block is cut by three faults F1, F2 and F3 which are represented by triangulated surfaces in Fig. 32. The F1 fault cuts the whole block and flattens in depth. The F2 fault branches on F1, and the F3 fault branches on F2 and F1. The hierarchical tree of the fault junctions which is used to build the junction enrichment, see Sect. 3.3, is shown in Fig. 33.

Boundary conditions are given in Fig. 34. The extension $\frac{\Delta u}{L}$ applied on the right border is set to 10 %. To eliminate any rigid body movement, the displacements perpendicular to the right wall and to the back and front walls are prohibited.

For the sake of simplicity, this example is aimed at capturing only the first order kinematics resulting from the large sliding along the fault surfaces and the associated folding of bulk material. Gravity is not accounted for and, as a consequence, a zero initial stress state is assumed. Also, assuming finite rotations but small strains, the material is represented by a Kirchhoff–St. Venant hyperelasticity with Young's modulus set to 2.5 GPa and Poisson's ratio set to 0.3. Note that because the model is not scaled with respect to gravity, the arbitrary choice of the value of Young's modulus has no consequence. Finally, to ensure material continuity, frictionless bilateral contact is enforced on the fault surfaces, so that contact is satisfied independently of the sign of the contact reaction. This assumption is useful to model the absence of gravity, that normally sets automatically the surfaces under compression.

6.3.2 Results

Figure 35 shows the final state of the simulation. The extension imposed on the right border of the model is first accommodated by a large sliding on F1 which induces the folding of the upper material due to F1 curvature. This folding is responsible for an extension in the outer-arc. In a real sedimentary basin, such an extension is susceptible to trigger the formation of opening fractures which facilitates the hydrocarbon flow. We will not develop further this interpretation because it should obviously require the model to be scaled with respect to gravity. However, this model shows that the branching of faults in 3D is adequately captured by the X-FEM approach, as can be noticed by the separation of the outer-arc in two domains, with a small stair step associated to sliding along the F2 fault.

7 Conclusion and prospects

An extension of the X-FEM approach has been presented in order to take into account branched discontinuities with possible large sliding contact conditions. The enrichment definition generalizes the one of [8] to the case of an arbitrary hierarchy of junctions between the discontinuities. An extension of the vital edge approach of [17] and [4] satisfying the LBB condition has been proposed for the junction zones. A simple example demonstrates a linear convergence of the relative error in the strain energy with the mesh refinement, and a superlinear convergence of the relative error in the contact pressure. The robustness of the method is ensured by means of an adequate conditioning strategy. A stiffness criterion has been proposed and a way is given to apply the orthogonalization proposed by [3] for the Heaviside enrichment. A 2D example shows the ability of branching with X-FEM to compute correct stress intensity factor prediction when compared to the semi-analytical approach of [41]. The present method improves earlier results of [28] and complete the results by adding the possibility of contact. Finally, a 3D example of the formation of a geological graben illustrates the capability of the method to capture complex kinematics with large sliding along branching discontinuities.

This work should open new perspectives for problems with X-FEM. It could also be completed by taking into account the frictional non linearity together with the bulk material non linearity and gravity effects.

Acknowledgments This work has been realized during a three-years doctoral thesis of the first author at the Geology–Geophysics–Geochemistry Division of IFPEN. The developments have been implemented within the software Code_Aster (version 10.* 11.0) which is a general software for the study of the mechanical behavior of structures distributed by EDF R&D under a GNU GPL license on the website http://www.code-aster.org. The final deformations of the numerical examples were illustrated with GNU GPL software Gmsh available at http://www.geuz.org.

References

1. Alart P, Curnier A (1991) A mixed formulation for frictional contact problems prone to Newton like solution methods. Comput Methods Appl Mech Eng 92:353–375
2. Babuška I (1973) The finite element method with Lagrangian multipliers. Numer Math 20(3):179–192
3. Béchet E, Minnebo H, Moës N, Burgardt B (2005) Improved implementation and robustness study of the X-FEM for stress analysis around cracks. Int J Numer Methods Eng 64(8):1033–1056
4. Béchet E, Moës N, Wohlmuth B (2009) A stable Lagrange multiplier space for stiff interface conditions within the extended finite element method. Int J Numer Methods Eng 78(8):931–954
5. Ben Dhia H, Zarroug M (2002) Hybrid frictional contact particles-in elements. Eur J Comput Mech 11:417–430
6. Brezzi F, Fortin M (1991) Mixed and hybrid finite element methods. Spriner, New York
7. Chapelle D, Bathe KJ (1993) The inf-sup test. Comput Struct 47(4/5):537–545
8. Daux C, Moës N, Dolbow J, Sukumar N, Belytschko T (2000) Arbitrary branched and intersecting cracks with the extended finite element method. Int J Numer Methods Eng 48:1741–1760
9. Destuynder P, Djaoua M (1981) Sur une Interprétation Mathématique de l'Intégrale de Rice en Théorie de la Rupture Fragile. Math Methods Appl Sci 3(1):70–87
10. Dolbow J, Moës N, Belytschko T (2001) An extended finite element method for modeling crack growth with frictional contact. Comput Methods Appl Mech Eng 190:6825–6846
11. Duarte CA, Reno LG, Simone A (2007) A high-order generalized FEM for through-the-thickness branched cracks. Int J Numer Methods Eng 72:325–351
12. Dulac JC, Gringarten E (2011) Approach couples fluid flow, Geomechanical simulations in 3-D reservoir modeling. The American Oil & Gas Reporter
13. Dumont G (2001) Algorithme des contraintes actives et contact unilatéral sans frottement. Euro J Comput Mech 4(1):55–73
14. Erdogan F, Sih G (1963) On the crack extension in plates under plane loading and transverse shear. Trans ASME J Basic Eng 85(2):519–527
15. Gosz M, Moran B (2002) An interaction energy integral method for computation of mixed-mode stress intensity factors along non-planar crack fronts in three dimensions. Eng Fract Mech 69: 299–319
16. Géniaut S, Massin P, Moës N (2005) Fissuration avec X-FEM et contact. In: Actes du 7ème Colloque National en Calcul des Structures, Giens
17. Géniaut S, Massin P, Moës N (2007) A stable 3D contact formulation for cracks using X-FEM. Eur J Comput Mech 16(2):259–275
18. Khoei AR, Nikbakht M (2006) Contact friction modeling with the extended finite element method (X-FEM). J Mater Process Technol 177:58–62
19. Laborde P, Pommier J, Renard Y, Salaün M (2005) High-order extended finite element method for cracked domains. Int J Numer Methods Eng 64(3):354–381
20. Lasserre JB (1998) Integration on a convex polytope. Proc Am Math Soc 126(8):2433–2441
21. Lepage F (2003) Génération de maillages tridimensionnels pour la simulation des phénomènes physiques en géosciences. PhD thesis, Institut National Polytechnique de Lorraine
22. Liu F, Borja R (2008) A contact algorithm for frictional crack propagation with the extended finite element method. Int J Numer Methods Eng 76:1489–1512
23. Moës N, Dolbow J, Belytschko T (1999) A finite element method for crack growth without remeshing. Int J Numer Methods Eng 46:131–150
24. Moës N, Gravouil A, Belytschko T (2002) Non-planar 3D crack growth by the extended finite element and level sets—part I: mechanical. Int J Numer Methods Eng 53:2549–2568
25. Moës N, Béchet , Tourbier M (2006) Imposing Dirichlet boundary conditions in the extended finite element method. Int J Numer Methods Eng 67(12):1641–1669
26. Mourad HM, Dolbow J, Harari I (2007) A bubble-stabilized finite element method for Dirichlet constraints on embedded interfaces. Int J Numer Methods Eng 69(4):772–793
27. Mousavi SE, Sukumar N (2011) Numerical integration of polynomials and discontinuous functions on irregular convex polygons and polyhedrons. Comput Mech 47(5):535–554
28. Mousavi S, Grinspun E, Sukumar N (2010) Higher-order extended finite elements with harmonic enrichment functions for complex crack problems. Int J Numer Methods Eng 86(4-5):560–574
29. Nistor I, Guiton MLE, Massin P, Moës N, Géniaut S (2009) An X-FEM approach for large sliding contact along discontinuities. Int J Numer Methods Eng 78(12):1407–1435

30. Nuismer R (1975) An energy release rate criterion for mixed mode fracture. Int J Fract 11(2):245–250
31. Pierrès E, Baietto MC, Gravouil A (2010) A two-scale extended finite element method for modelling 3D crack growth with interfacial contact. Comput Methods Appl Mech Eng 199(17-20): 1165–1177
32. Rice JR (1968) A path independent integral and the approximate analysis of strain concentration by notches and cracks. J Appl Mech 35:379–386
33. Sanders JD, Dolbow JE, Laursen TA (2009) On methods for stabilizing constraints over enriched interfaces in elasticity. Int J Numer Methods Eng 78:1009–1036
34. Stern M, Becker EB, Dunham RS (1976) A contour integral computation of mixed-mode stress intensity factors. Int J Fract 12(3):359–368
35. Siavelis M, Massin P, Guiton MLE, Mazet S, Moës N (2010) Robust implementation of contact under friction and large sliding with the eXtended finite element method. Eur J Comput Mech 19(1-2-3):189–203
36. Sih G (1974) Strain-energy-density factor applied to mixed mode crack problems. Int J Fract 10:305–321
37. Simone A, Duarte CA, Vander Giessen E (2006) A generalized finite element method for polycrystals with discontinuous grain boundaries. Int J Numer Methods Eng 67:1122–1145
38. Solberg JM, Papadopoulos P (2005) An analysis of dual formulations for the finite element solution of two-body contact problems. Comput Methods Appl Mech Eng 194:2734–2780
39. Ventura G (2006) On the elimination of quadrature subcells for discontinuous functions in the eXtended finite-element method. Int J Numer Methods Eng 66:761–795
40. Wriggers P (2002) Computational contact mechanics. Wiley, New York
41. Yavuz A, Phoenix S, TerMaath S (2006) Multiple crack analysis in finite plates. AIAA J 44(11):2535–2541